Comprehensive Evaluation of Toroid Ring Core Parallel Inductor and Resistor as a Transformer Protection Device

Heidary, Amir; Ghaffarian Niasar, Mohamad; Popov, Marjan

DOI
10.1109/TCSI.2024.3428363

Publication date
2024

Document Version
Final published version

Published in
IEEE Transactions on Circuits and Systems I: Regular Papers

Citation (APA)
Heidary, A., Ghaffarian Niasar, M., & Popov, M. (2024). Comprehensive Evaluation of Toroid Ring Core Parallel Inductor and Resistor as a Transformer Protection Device. *IEEE Transactions on Circuits and Systems I: Regular Papers*, *71*(9), 4298-4308. https://doi.org/10.1109/TCSI.2024.3428363

Comprehensive Evaluation of Toroid Ring Core Parallel Inductor and Resistor as a Transformer Protection Device

Amir Heidary, *Senior Member, IEEE*, Mohamad Ghaffarian Niasar, *Member, IEEE*, and Marjan Popov, *Fellow, IEEE*

***Abstract*— The energy transition involves integrating numerous pieces of equipment that undergo frequent switching operations and face the risk of lightning strikes. Consequently, power systems are exposed to fast transient switching and lightning surges, necessitating enhanced protection solutions for power equipment. Over the past decade, viable solutions have emerged to mitigate fast transients and safeguard transformers in the form of a ring-core parallel inductor and resistor circuit (R-PIR). Although this device effectively protects medium-voltage transformers from fast transients, a precise and comprehensive model for this component is still lacking, especially considering the importance of refining the R-PIR for broader applications. This paper introduces a detailed model of the R-PIR as a protective device, validated by electromagnetic transient simulations and finite element methods, which are also confirmed by experiments. The main goals of the research work are to investigate the performance and design features of the R-PIR comprehensively and demonstrate how the designed R-PIR protects transformers against fast transients. The research work is validated by experiments conducted in a lab environment. It is concluded that designing the R-PIR within an appropriate frequency range can considerably suppress transient overvoltages to which the transformer is exposed.**

***Index Terms*— Fast transients, transformer resonances, protection, protection device, resonances.**

I. Introduction

FAST transient (FT) phenomena in power systems occur due to lightning strikes or circuit breaker switching [1], [2]. By integrating more renewable generators, the number of switching actions and lightning strikes to the towers increases, and so does the FTs [3]. Even though the power grid are exposed to different transient waveforms, in this paper, FT analysis refers to the standard lightning impulse (IEC 61000), which is a voltage transient and includes various harmonic contents [4].

FTs in power systems influence the operation of the power equipment, in particular, transformers, by causing resonance and overvoltages [5]. FTs include various harmonic contents, and therefore, they are the source of resonance and may damage the transformer insulation [6].

Several devices have been presented to protect high-power transformers against FTs [6]. These protection devices are the surge arresters [7], surge capacitors and RC snubbers [8], ZnO arrester RC (ZORC) [9], pre-insertion resistors (PIRs) [10], [11], and ring core suppressors [12]. Even though these protection devices are effective against transient overvoltage suppression, the ring core parallel inductor and resistor circuit (R-PIR) is a series-protection device that is tested in the power grid, offering several benefits like filtering transient signal harmonic content and they do no need to be grounded [13], [14]. It is a relatively simple structure comprising a ferromagnetic core, a conductor, and a resistive secondary suppressor [15]. This component is connected in series with the protected transformer, such as those used in wind farms [16], and is capable of suppressing the FTs, to which transformers are exposed, as reported in [17] and [18]. Additionally, ring magnetic cores are applied to cables or overhead lines and gas insulated cables to suppress lightning transients as reported in [12] and [20]. Experience shows that the concept of a parallel RL circuit connected in series with the overhead line or cable is a well-known idea to suppress voltage transient oscillations [21], [22]. Besides, the choke has been presented as an RL circuit in [23] and [24], however, it has not been sufficiently studied.

In this paper, a detailed R-PIR model of a choke is developed by applying finite element method (FEM), and electromagnetic transient (EMT) simulations; afterward, the simulation results are validated by experiments. In the last phase, the high-voltage impulse testing of the R-PIR is conducted to validate its performance for protecting a laboratory low-power HV transformer and suppressing transient oscillations. The main contributions of this paper are:

- A comprehensive evaluation of R-PIR, including FEM and EMTP analysis, frequency domain analysis, and high-voltage testing,
- Determination of detailed parameters for the design of different cases,

Manuscript received 31 March 2024; revised 15 June 2024; accepted 10 July 2024. Date of publication 22 July 2024; date of current version 29 August 2024. This work was supported by the Nederlandse Organisatie voor Wetenschappelijk Onderzoek (NWO) in collaboration with Transmission System Operator (TSO) TenneT, Distribution System Operator (DSO) Alliander, Royal Smit Transformers, and TSO National Grid, U.K., in the Framework of the NWO-Toegepaste en Technische Wetenschappen (TTW) Project "Protection of Future Power System Components" under Grant 18.699. This article was recommended by Associate Editor X. Wang. *(Corresponding author: Amir Heidary.)*

The authors are with the Faculty of Electrical Engineering, Mathematics and Computer Science (EEMCS), Delft University of Technology, 2628 CD Delft, The Netherlands (e-mail: A.Heidary@tudelft.nl; M.GhaffarianNiasar@tudelft.nl; M.Popov@tudelft.nl).

Color versions of one or more figures in this article are available at https://doi.org/10.1109/TCSI.2024.3428363.

Digital Object Identifier 10.1109/TCSI.2024.3428363

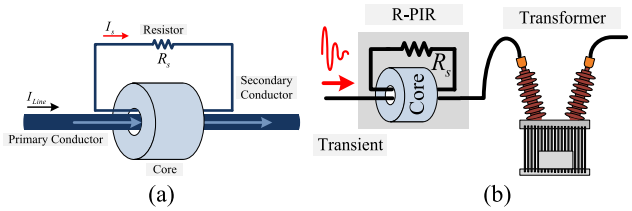

Fig. 1. a) R-PIR structure, b) the series connection of an R-PIR with a transformer.

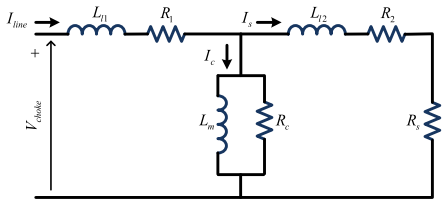

Fig. 2. Low-frequency equivalent circuit of the R-PIR.

- Investigation of the R-PIR's performance by analyzing its magnetic and electric field distribution,
- Black box frequency sweep circuit modeling and validation,
- Conducting high-voltage tests to examine the designed R-PIR effects on transient oscillation suppression

The rest of the paper is organized as follows. Section II deals with the configuration and operation of the R-PIR. Section III explains the modeling procedure of R-PIR. Section IV and Section V elaborates on the FEM and EMT analysis respectively. Experimental research work is comprehensively presented in Section VI and finally, meaningful conclusions are summarized in Section VII.

II. R-PIR Configuration and Operation

As an FT suppressor, the R-PIR, as a two-winding component, is connected in series with the transformer to protect it against overvoltages and resonances that may occur due to FTs. This device comprises a core, a primary conductor, secondary turns, and a resistor. Fig. 1 illustrates the structure of the R-PIR and its connection to the transformer.

As shown in Fig. 1 (a), a part of the line conductor passes through the core, being the R-PIR's primary turn, while the secondary turn is wounded around the core, being the suppression section. Moreover, the resistor R_s is connected to the secondary winding to suppress the transient signal resulting from a secondary current. Fig. 1 (b) shows the R-PIR connection to the transformer to protect it against FTs.

The operation modes of the R-PIR can be divided into two stages. The first operation mode of the R-PIR is active during the power system frequency when there is no FT signal. In this stage, the R-PIR's impedance is negligibly low. The second operation mode of the R-PIR deals with FTs and their high-frequency content. In this mode, the magnitude of the high-frequency content of the FT decreases due to the voltage drop of the R-PIR, and upon operation, the transformer's resonance overvoltage will not occur.

III. R-PIR Modeling

The R-PIR can be considered a series transformer in which the resistor is in its secondary circuit. However, for higher frequencies, the modeled circuit will be more comprehensive, considering the capacitive effects of the conductors. Therefore, the analysis is first applied considering the power system frequency operation to investigate the R-PIR low-frequency model. Next, the analysis of the R-PIR high-frequency model is carried out considering the interaction of R-PIR and FTs. The main purpose of this section is to provide equations to compute all the parameters of R-PIR so that in the next step, these parameters can be used for the simulation of R-PIR to demonstrate its performance.

A. R-PIR Power System Frequency Analysis

The ratio of the R-PIR is one and it can be represented by a transformer equivalent scheme that can correctly define the behavior of the R-PIR for a power system frequency. In this scheme, only the resistances and inductances are considered, whilst the insulation and capacitive behavior can be neglected (because of their very high impedance at a low frequency). Fig. 2 shows the power system frequency model of the R-PIR. This model can be used for power loss analysis of the R-PIR during steady-state operation.

In the illustrated circuit of Fig. 2, L_{l1} and L_{l2} are the leakage inductances of the R-PIR for the primary and the secondary side, while R_1 and R_2 are the primary and secondary resistance, respectively. L_m is the R-PIR's magnetizing inductance, and R_c is the modeled resistance of the core where the turns ratio is 1:1. The total impedance of the R-PIR, Z_c, and R-PIR voltage drop $V_{\text{R-PIR}}$ can be computed by (1) and (2).

$$Z_c = R_1 + j\omega L_{l1} + (R_c || j\omega L_m || (R_2 + R_s + j\omega L_{l2})) \tag{1}$$

$$V_{\text{R-PIR}} = I_{line}\,(R_1 + j\omega L_{l1} + (R_c || j\omega L_m || (R_2 + R_s + j\omega L_{l2}))) \tag{2}$$

By applying Kirchhoff's Current Law (KCL), the current in each branch can be computed as follows:

$$I_{line} = I_c + I_s \tag{3}$$

$$I_c = \frac{V_{\text{R-PIR}} - (I_{line}(R_1 + j\omega L_{l1}))}{R_c.j\omega L_m / R_c + j\omega L_m} \tag{4}$$

$$I_s = \frac{V_{\text{R-PIR}} - (I_{line}(R_1 + j\omega L_{l1}))}{R_2 + R_s + j\omega L_{l2}} \tag{5}$$

Here, I_{line}, I_c, I_s are the currents of the power line, core branch, and secondary side, respectively. Considering the current of each branch, power loss P_{loss} of R-PIR for a power system frequency can be determined as follows:

$$P_{loss} = P_p + P_c + P_s \tag{6}$$

$$P_p = I_{line}^2 R_1 \tag{7}$$

$$P_c = \frac{(V_{\text{R-PIR}} - (I_{line}(R_1 + j\omega L_{l1})))^2}{R_c} \tag{8}$$

$$P_s = (R_2 + R_s)\left(\frac{V_{\text{R-PIR}} - (I_{line}(R_1 + j\omega L_{l1}))}{R_2 + R_s + j\omega L_{l2}}\right)^2 \tag{9}$$

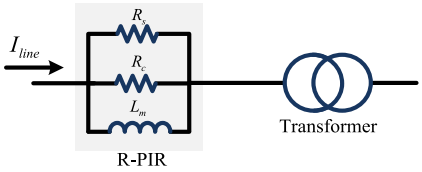

Fig. 3. Simplified equivalent circuit of the R-PIR (for power frequency analysis).

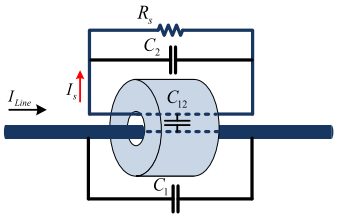

Fig. 4. Considered capacitance in R-PIR structure.

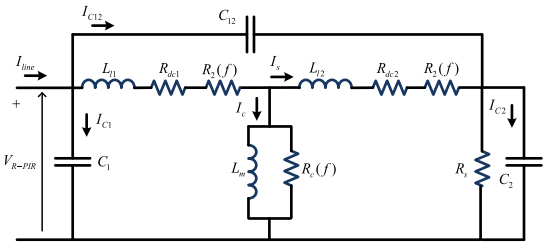

Fig. 5. High-frequency equivalent circuit of R-PIR.

The cross-section of the conductors and core should be increased to decrease the power loss of the R-PIR during steady-state operation. Moreover, power loss can be decreased by decreasing resistance R_s.

Reactive power consumption Q of the R-PIR for a power frequency can be determined as follows:

$$Q = Q_p + Q_c + Q_s \tag{10}$$

$$Q_p = I_{line}^2 j\omega L_{l1} \tag{11}$$

$$Q_c = \frac{(V_{\text{R-PIR}} - (I_{line}(R_1 + j\omega L_{l1})))^2}{j\omega L_m} \tag{12}$$

$$Q_s = (j\omega L_{l2}) \left(\frac{V_{\text{R-PIR}} - (I_{line}(R_1 + j\omega L_{l1}))}{R_2 + R_s + j\omega L_{l2}} \right)^2 \tag{13}$$

To decrease the reactive power consumption, the cross-section of the core should be decreased accordingly, considering that the leakage inductance value is much smaller than the magnetizing inductance.

By applying the following condition to the equivalent circuit of the R-PIR, its equivalent circuit is simplified.

$$R_2 + j\omega L_{l2} \ll R_s \tag{14}$$

$$R_1 + j\omega L_{l1} \ll j\omega L_m || R_c || R_s \tag{15}$$

According to (14) and (15), L_{l1}, R_1, L_{l2}, and R_2 can be ignored from the equivalent circuit, and the final R-PIR model for power frequency analysis can be represented by an R-L shunt circuit, as illustrated in Fig.3.

B. R-PIR High-Frequency Analysis

Various harmonic contents are generated during FT state, and the R-PIR will protect the transformer by suppressing these harmonic contents. Therefore, the R-PIR's high-frequency model is essential for the design of a practical protection device. Each electrical element of the R-PIR should be considered to provide an accurate high-frequency model of the R-PIR.

Concerning the high-frequency model, the capacitive terms of the R-PIR are the capacitances of primary terminal C_1, secondary terminal C_2, and primary to secondary conductor C_{12}. These capacitances are shown in Fig. 4.

This model assumes that the capacitances of the conductors to the ground are very low because of the large distance between the conductors and the ground.

The resistances of the primary and secondary conductors are also essential for the high-frequency model. These resistances include two terms, DC resistances R_{dc1} and R_{dc2}, and frequency-dependent resistances $R_1(f)$ and $R_2(f)$. Besides, the resistance of the core is also a function of the frequency. The high-frequency model of the R-PIR is depicted in Fig. 5. Furthermore, regarding the operation frequency range of R-PIR (mostly around 10 kHz to 1 MHz) and the length of R-PIR (around 200 mm), the wavelength is much larger than the R-PIR length. Consequently, the amount of magnetic field emission is negligible, and therefore, the lumped-parameter representation of R-PIR is suitable.

The impedance of the R-PIR and its voltage drop depending on the frequency according to the equivalent circuit shown in Fig. 5 can be determined by the following expressions:

$$Z_1 = R_{dc1} + R_1(f) + j\omega L_{l1} \tag{16}$$

$$Z_2 = R_{dc2} + R_2(f) + j\omega L_{l2} \tag{17}$$

$$Z_{core} = R_c || j\omega L_m \tag{18}$$

$$Z_{AB} = \frac{Z_1.Z_2 + Z_2.Z_{core} + Z_{core}.Z_1}{Z_{core}} \tag{19}$$

$$Z_{BC} = \frac{Z_1.Z_2 + Z_2.Z_{core} + Z_{core}.Z_1}{Z_1} \tag{20}$$

$$Z_{CA} = \frac{Z_1.Z_2 + Z_2.Z_{core} + Z_{core}.Z_1}{Z_2} \tag{21}$$

$$Z_c = \left(Z_{CA} || \frac{1}{j\omega C_1} \right) || \left(\left(Z_{AB} || \frac{1}{j\omega C_{12}} \right) + \left(Z_{BC} || \frac{1}{j\omega C_2} \right) \right) \tag{22}$$

$$V_{\text{R-PIR}} = I_{line} \left(\left(Z_{CA} || \frac{1}{j\omega C_1} \right) || \left(\left(Z_{AB} || \frac{1}{j\omega C_{12}} \right) + \left(Z_{BC} || \frac{1}{j\omega C_2} \right) \right) \right) \tag{23}$$

To calculate the R-PIR's impedance, Z_1, Z_2, and Z_{core} are first computed to simplify the circuit components, and then Z_{AB}, Z_{BC}, and Z_{CA} are applied to compute star-connected impedances to delta impedances. By taking into account (22), the R-PIR can provide a remarkable impedance against the high-frequency content of the FTs. Consequently, the magnitude of the high-frequency signal can be suppressed by its

voltage drop, as shown in (23), and the transformer will be protected against FT accordingly.

C. R-PIR R-L-C Elements Calculation

1) Coke Resistance and Secondary Energy Calculation: In the R-PIR design, the DC resistances of the primary and secondary conductors (frequency-independent resistance) depend on the conductors' conductance, length, and cross-section. Therefore, the expression for DC resistance computation can be written as follows:

$$R_{dc1} = \frac{l_p}{\sigma S_p} \tag{24}$$

$$R_{dc2} = \frac{l_s}{\sigma S_s} \tag{25}$$

In this equation, the conductance of both primary and secondary σ are considered the same. l_p and l_s refer to the lengths of the primary and secondary conductors passing through the core, respectively. They take into account the fringing field effect at the edges of the R-PIR (as per the FEM model); this includes an additional length of b/4, where b is the core radius. S_p and S_s are the cross-sections of the primary and secondary conductors.

Expressions [16] and [17] represent the R-PIR's frequency-dependent resistance related to the skin effect depth and proximity effect. The resistances $R_1(f)$ and $R_2(f)$ can be computed according to (26):

$$R_{1,2}(f) = R_{dc1,2}\left(\begin{array}{l} Re\left\{\sqrt{j2\pi f\mu_0\sigma\frac{d_{1,2}}{t}\sqrt{\frac{\pi}{4}}}.d\coth(d)\right\} \\ +Re\left\{2\sqrt{j2\pi f\mu_0\sigma\frac{d_{1,2}}{t}\sqrt{\frac{\pi}{4}}}.d\tanh(d/2)\right\}\end{array}\right) \tag{26}$$

where f is the transient oscillation frequency, μ_0 is the magnetic permeability of the conductor, $d_{1,2}$ is the diameter of the primary or secondary conductor, and t is the distance between the conductors' centers. Moreover, in this equation, "Re" refers to the real part of the complex expression provided in the brackets. W_D is the transferred energy to the R-PIR's secondary resistor and is computed by (27). This energy must be dissipated by the appropriate design of the secondary resistor's size and material. Here, the transient voltage oscillation $v_{(t)}$ is assumed to be linear and consists of two regions (rising and falling). t_0 is the time when the transient oscillation occurs, and t_1 is the end of the rising trend of the transient oscillation. t_1 is also the time when the transient oscillation starts decreasing, and t_2 is the end of the transient oscillation. Furthermore, m_r and m_f are the rates of the rising and decreasing of the transient oscillation, respectively, and R_s is the resistor of the secondary winding.

$$W_D = \int_{t0}^{t1}\frac{m_r v_{(t)}^2}{R_s}dt + \int_{t1}^{t2}\frac{m_f v_{(t)}^2}{R_s}dt \tag{27}$$

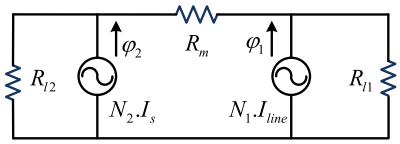

Fig. 6. The R-PIR magnetic equivalent circuit.

2) R-PIR Inductance Calculation: Considering the R-PIR as a linear device, the component's leakage and magnetizing inductance can be computed by (28)-(30). By taking into account that the number of primary and secondary turns (N_1 and N_2) of the R-PIR is one, the inductances L_{l1}, L_{l2}, and L_{m} are only functions of associated reluctances.

$$L_{l1} = \frac{N_1^2}{R_{l1}} = \frac{1}{R_{l1}} \tag{28}$$

$$L_m = \frac{N_1.N_2}{R_m} = \frac{1}{R_m} \tag{29}$$

$$L_{l2} = \frac{N_2^2}{R_{l2}} = \frac{1}{R_{l2}} \tag{30}$$

These equations are derived by using the equivalent magnetic circuit of the R-PIR shown in Fig. 6, where R_{l1}, R_{l2}, are the leakage air and core reluctances, respectively.

In this circuit, the reluctance of the only core R_m is frequency-dependent. However, ferrite cores are particularly affected at a frequency higher than 100 kHz. This means that the R-PIR inductances can be considered frequency-independent for a frequency range between 10-100 kHz, which are the main operating frequencies of the R-PIR. These reluctances can be computed as follows:

$$R_{l1} = \frac{l_{a1}}{A_{a1}.\mu_0} \tag{31}$$

$$R_m = \frac{l_c}{A_c.\mu_c} \tag{32}$$

$$R_{l2} = \frac{l_{a2}}{A_{a2}.\mu_0} \tag{33}$$

Here, l_{a1} and l_{a2} are the average lengths of the leakage flux paths in the air, and A_{a1} and A_{a2} are the average cross-sections of the leakage flux direction. l_c is the average length of the core, and, μ_0 and μ_c are the air and core permeability, respectively.

3) R-PIR Capacitances Calculation: In the R-PIR structure, it is possible to model various capacitances between conductors. However, regarding the value of the capacitors, the largest one in each section can provide the model of the R-PIR. Regarding this assumption, the capacitance between the primary and secondary conductor, the primary terminal and the secondary terminal can be calculated.

D. The Capacitance Calculation Between Primary and Secondary Conductors

This subsection deals with the determination of the capacitances of the primary and secondary conductors of the R-PIR. The assumption here is that the core as an equipotential surface is ignored because of its distance from the conductors

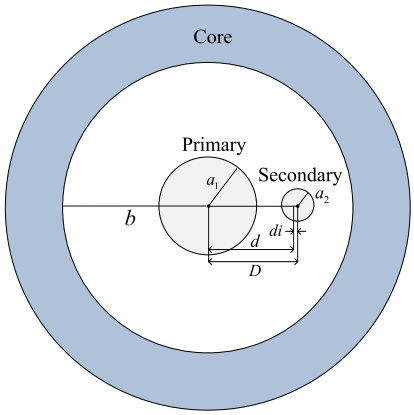

Fig. 7. Geometry of primary and secondary conductor inside the core.

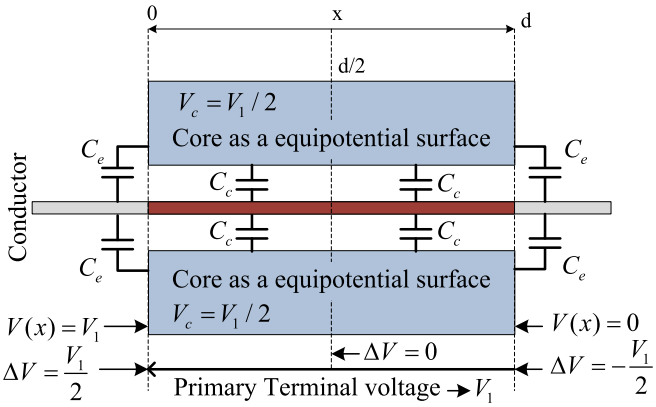

Fig. 8. The R-PIR magnetic equivalent circuit.

($b \gg d$-($a_1 + a_2$)). To calculate the capacitance between the primary and secondary conductor the geometry shown in Fig. 7 is used. These two conductors are considered parallel cylinders inside the core, and the capacitance can be calculated by (34), where a_1 and a_2 are the radii of the primary and secondary conductors, and d is the distance between their centers.

$$C_{12} = 2\pi\varepsilon_0 d \big/ (\ln a_1/d - \ln a_2/d) \tag{34}$$

Here, ε_0 is the permittivity of the conductor, which is roughly equal to the permittivity of the air. C_{12} is obtained in F/m.

E. The Capacitance Calculation of the Primary Terminal

The next step is to determine the terminal capacitance of the primary and secondary turn of the R-PIR. The capacitance of the primary terminal is calculated according to Fig. 8.

To calculate the capacitance of the primary terminal, it is assumed that the core is an equipotential surface where the voltage V_c to ground is half of the R-PIR primary conductor voltage drop V_1, and the secondary conductor has a negligible impact. V is the voltage distribution along the primary conductor, which varies from V_1 to *0*.

As illustrated in Fig. 8, the capacitance value between the piece of conductor covered by the core C_c is larger than the edge capacitances C_e. This assumption is shown by (35) and (36).

$$\sum C_c \gg \sum C_e \tag{35}$$

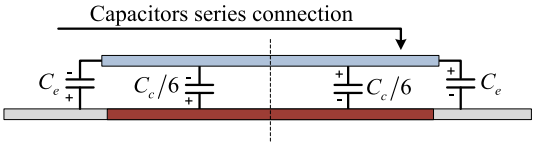

Fig. 9. Equivalent circuit for R-PIR primary capacitance calculation.

$$V_c = V_1/2 \tag{36}$$

Voltage differences between the core and each point of the conductor are defined as ΔV and expressed by (37). The voltage distribution $V(x)$ along the conductor to the ground is a function of distance x (which varies between 0 and d) and is represented by (38).

$$\Delta V(x) = V(x) - V_c \tag{37}$$

$$V(x) = V_1 - x \tag{38}$$

In the first step, the capacitance of the primary terminal is calculated to determine the capacitance of the cylindrical conductor and the core which shields the conductor. This capacitance is calculated by (39) assuming a unified electric field in space between the conductor and core.

$$C_c = 2\pi\varepsilon_0 d \big/ \ln(b/a) \tag{39}$$

In (39), it is assumed that the voltage differences between the conductor and core ΔV are equal at each point, which shows that the electric field between the inner and outer cylinders is homogenous. However, in the R-PIR, this is not the case, and the voltage is distributed between the conductor and core. This condition is considered for the calculation of the terminal capacitance by using the stored electrical energy equation as expressed by (40).

$$W_e = \frac{1}{2}\int_0^d C_c\,(\Delta V(x))^2\,dx \tag{40}$$

By solving (40), considering that d is the length of the core, the stored energy in the capacitances of the R-PIR will be calculated by the presented equation in(41).

$$2W_e = C_c/3 \tag{41}$$

In the next step, by focusing on the polarity of the voltage between the primary conductor and core, it is clear that the capacitance of half of the horizontal length of the R-PIR (d/2) is connected in series with another half of the R-PIR. Therefore, the capacitance of the R-PIR for the primary terminal can be expressed by (42).

$$C_1 = \pi\varepsilon_0 d/6 \ln(b/a) + C_e/2 \tag{42}$$

This equation can be derived by taking into account the equivalent circuit, which is illustrated in Fig. 9.

F. The Capacitance Calculation of the Secondary Terminal

The capacitance of the secondary terminal of the R-PIR is calculated by taking into account that the distance between the primary and secondary conductor is shorter than the distance

TABLE I
PARAMETERS OF SIMULATED R-PIR

Parameter	value
Core length	200 mm
Core radius	34 mm
Core thickness	10 mm
Primary conductor radius	1 mm
Secondary conductor radius	0.2 mm
Core permeability	2000
Core material	VITROPERM
Core Electrical conductivity	0.4 m/Ωmm^2
Secondary turn resistance	3 kΩ
Core material	Ferrite
Conductor material	Copper
Core maximum saturation flux density	1200 mT
Applied voltage to the primary	1 p.u.
Applied current to primary (normal state)	100 A
Applied current to primary (transient oscillation state)	100 A

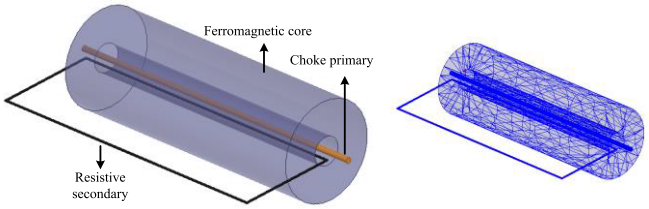

Fig. 10. a) 3D geometric design of R-PIR, b) mesh plot of R-PIR.

between the secondary conductor and core. The capacitance between the primary and secondary conductor is calculated by (39), and then the energy method with a series connection of the capacitors along the conductor is applied. The secondary terminal capacitance can be determined as:

$$C_2 = \pi \varepsilon_0 d/6 \left(\ln a_1/d - \ln a_2/d\right) + C_e/2 \qquad (43)$$

IV. FEM ANALYSIS OF R-PIR

A. Design of Studied R-PIR in the FEM Platform

In this section, to evaluate R-PIR's specifications, the geometry of the R-PIR is programmed in an FEM environment. The geometric size of the R-PIR is based on the analytical studies reported in Section II. Two constraints should be taken into account when designing R-PIR. First, there is a minimal impact in steady-state operation (very low voltage drop), and second, there is an acceptable impedance during transient oscillation to suppress its magnitude. Accordingly, Table I presents the parameters of the R-PIR used for the FEM analysis, including geometric data and material properties.

The FEM analysis confirms the following performances of R-PIR:

- Magnetic flux density in the core and core saturation aspects
- R-PIR's inductance and resistance
- Voltage distribution in the R-PIR structure and critical insulation regions
- The capacitance between the primary and secondary conductor of the R-PIR

Fig. 10 demonstrates the 3D model design of the R-PIR and the mesh plot of the geometry.

In this section, firstly, the performance of the core (considering magnetic flux density) is studied by exciting the primary

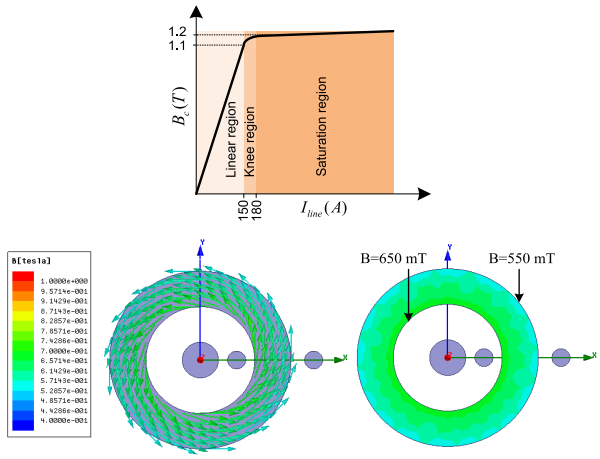

Fig. 11. a) B-I curve of the studied core, b) R-PIR magnetic flux density for a power frequency (50 Hz).

side with a steady-state and high-frequency current. Here, magnetic flux density distribution in the core presents the flux density value for each core section. Secondly, the voltage distribution of the R-PIR is presented to evaluate the capacitive model of the R-PIR and the critical points considering the insulation effects.

B. Magnetic Flux Density and R-PIR's Inductance for Steady-State and Transient Oscillation Operation

For the steady-state case, a 10 kV source, including its equivalent impedance, is connected in series to the primary terminal of the R-PIR. This case demonstrates that the R-PIR is connected to the power line where the steady-state peak current is 100 A. Hence, the performance of the R-PIR can be evaluated in a steady state. All FEM simulations are carried out by the transient solver supported by the FEM software tool.

Fig. 11 (a) shows the magnetic behavior of the studied core, and Fig. 11 (b) depicts the magnetic maximum flux density of the core for both 2D vector and magnitude plots. This simulation shows that the maximum magnetic flux density during steady-state in the R-PIR reaches 650 mT whilst the average magnetic flux density is 600 mT. The critical result is that during steady-state, the core is far from being saturated and is capable of suppressing fast transient oscillations during the faulty period. In the next case, a high-frequency source is applied with a crest voltage, which is twice as high as the steady-state system voltage at a frequency of 100 kHz. This simulation case demonstrates the core magnetic flux density in the R-PIR as the transient oscillation passes through it. This high-frequency source excites the primary turn of the R-PIR by 100 A. Fig. 12(a) shows the core's maximum magnetic flux density distribution. It can be observed that the magnetic flux density in the layer of the core closest to the primary conductor is 230 mT, while the outer layer's magnetic flux density is 20 mT. The huge difference in magnetic flux density in the core layers is because of the induced eddy currents during the high-frequency period. The average magnetic flux density in this state is 125 mT.

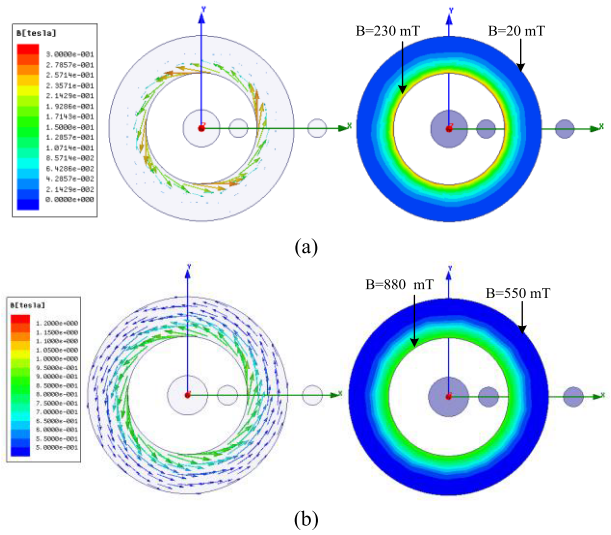

Fig. 12. R-PIR magnetic flux density for a frequency of 100 kHz.

Fig. 12(b) shows the distribution of the maximum magnetic flux density in the core, which shows the effects of the transient oscillation and steady-state line current on the R-PIR core, considering the current peak magnitude. It is found that the maximum magnetic flux density reaches 880 mT in the layer closest to the conductor, while the average magnetic flux density in the core cross-section is 725 mT.

Based on the FEM analysis, the R-PIR inductance of the primary terminal is 280 μH for the steady-state case and 259 μH for the transient oscillation case (excited at 100 kHz). Additionally, for the steady-state analysis, the conductor's leakage inductances for both the primary and secondary sides are 0.8 μH, and the resistances are 14 mΩ and 66 mΩ, respectively. When DC excitation is applied, the resistances are 12 mΩ and 65 mΩ. For a frequency of 100 kHz, the resistances of the primary and secondary sides increase to 27 mΩ and 98 mΩ, respectively. Moreover, by superimposing the values of the average flux density for the two frequencies (50 Hz and 100 kHz), the maximum average flux density is 725 mT, which is in the linear region of the saturation characteristic.

C. Voltage Distribution in the R-PIR

This study case considers the effect of the primary and secondary conductor, for which the voltage is (approximately) 1 V. Fig. 13 shows the voltage distribution in the R-PIR. By using the energy calculation method, the primary terminal capacitance of the R-PIR is determined as 60 pF.

The other obtained result from the simulation is that the external edge of the core and conductors experiences the highest electric potential, which should be taken into account for the insulation design. Moreover, the secondary terminal capacitance and the capacitance between the primary and secondary conductor are 80 pF and 68 pF, respectively.

V. EMTP Simulation of R-PIR

This section deals with the R-PIR's characteristics simulated by EMTP. Here, the presented equivalent circuit of the R-PIR, which is shown in Fig. 5, is used, and the parameters of the circuit elements are determined by applying the FEM analysis.

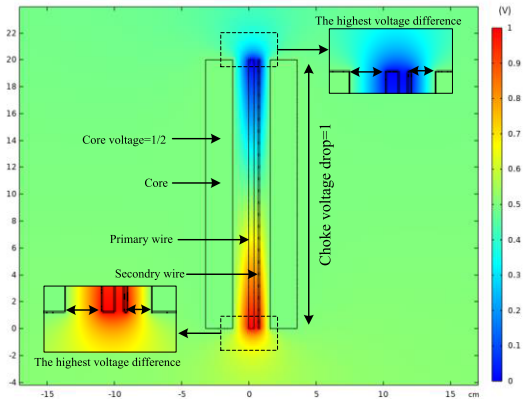

Fig. 13. R-PIR primary voltage distribution.

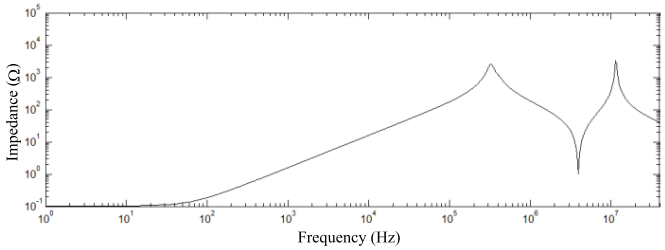

Fig. 14. R-PIR EMTP frequency-dependent impedance.

By using this equivalent circuit, the primary terminal frequency-dependent impedance of the R-PIR is obtained. Fig. 14 shows that the R-PIR impedance for low frequencies is very low, and it increases with the frequency increase, reaching approximately 1.3 kΩ around the first resonance frequency (220 kHz). It decreases to its minimum (12 Ω) at the next resonance point (30 MHz). This frequency-dependent characteristic shows that the R-PIR can provide an acceptable impedance within the range of 0.1MHz to 2MHz to successfully protect the transformer against resonances. Moreover, this resonance frequency can be changed based on the design of the R-PIR (considering the value of the capacitances and inductances).

VI. Experimental Evaluation of R-PIR

According to the performed analysis, an experimental test setup, shown in Fig. 15, is designed to study the R-PIR. The analysis is conducted by applying three types of tests. For the first test, the secondary R-PIR is open. The second test is carried out by having the secondary side of the R-PIR short-circuited, and the third test is carried out when R-PIR operates for an actual case.

The frequency sweep (FS) terminal impedance measurement is performed by using a Vector network analyzer (VNA) Bode 100 with a frequency range of up to 40 MHz. This device measures the R-PIR's frequency response by applying a current that is in the range of milliamperes. Therefore, its measurement is more valid when R-PIR works in linear regions.

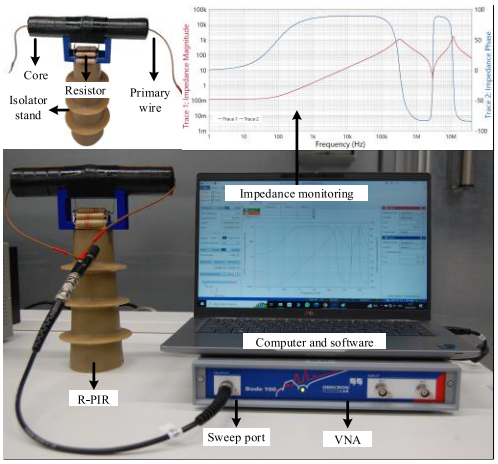

Fig. 15. Laboratory measurement setup.

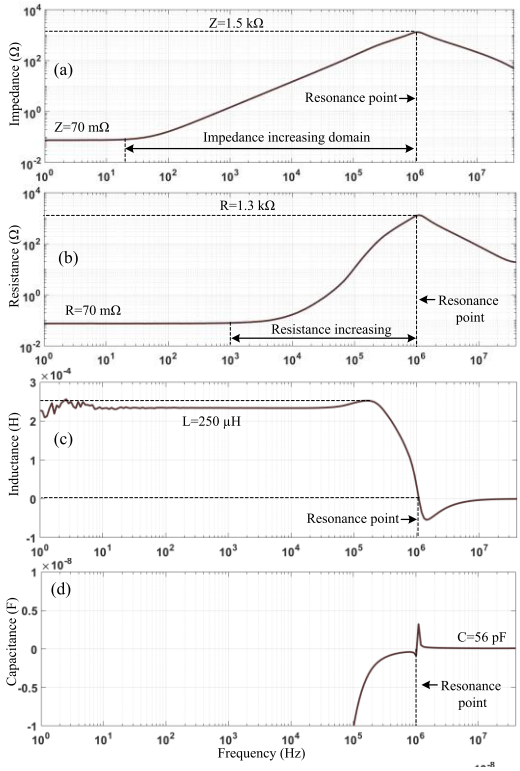

Fig. 16. R-PIR open-circuit FS a) terminal impedance, b) terminal resistance, c) terminal inductance, and d) terminal capacitance measurement.

The geometric data of the R-PIR for the laboratory test setup are presented in Table I. Impedance measurements are conducted using the VNA device to measure the impedance, resistance, inductance, and capacitance of the R-PIR within the frequency range of 1 Hz to 40 MHz. By selecting appropriate frequencies for each test, the values of the circuit parameters can be obtained. The obtained results are presented in Fig. 16 and Fig. 17.

A. R-PIR Open-Circuit Test

For the open-circuit test, the secondary of the R-PIR (suppressor resistor circuit) is open. The impedance of the primary terminal is measured in an FS mode. The effect of the secondary RLC circuit is negligible, and therefore, the remaining elements are the leakage and magnetizing inductance ($L_{l1} + L_m$), resistances (R_{dc1} and R_f), and capacitance (C_1) of the R-PIR primary side. Fig. 16 (a), (b), (c), and (d) shows the impedance, resistance, inductance, and capacitance of the primary R-PIR circuit. Overall, its impedance rises from 70 mΩ to 1500 Ω within the range of 20 Hz to 1 MHz (as a resonance point). Afterward, its impedance decreases till the next resonance point. The obtained data from this test are summarized in Table II.

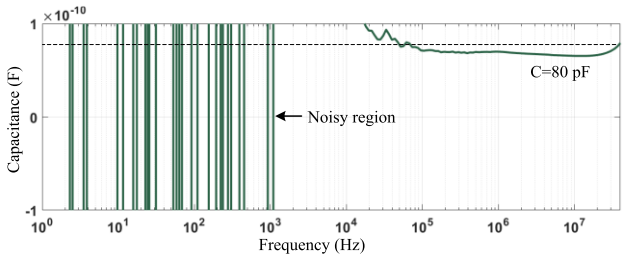

Fig. 17. R-PIR open-circuit FS capacitance measurement between primary and secondary terminals.

TABLE II
R-PIR PARAMETERS FOR THE OPEN-CIRCUIT TEST

Open-circuit FS measurement						
Measured parameter	L_m+L_{l1}	R_{dc1}	R_f (10kHz)	R_f (100kHz)	C_1	Z_c (max)
parameter value	250 µH	70 mΩ	0.2 Ω	10 Ω	56 pF	1.5 kΩ

TABLE III
R-PIR PARAMETERS FOR THE SHORT-CIRCUIT TEST

Short-circuit FS measurement						
Measured parameter	L_{l1}+L_{l2}	R_{dc1}+R_{dc2}	R (10kHz)	R_f (100kHz)	C_1	Z_c (max)
parameter value	1.8 µH	85 mΩ	0.095 Ω	0.1 Ω	55 pF	1 kΩ

As shown in Fig. 16 and Table II, by applying the open-circuit test, one can obtain the leakage and magnetizing inductance of the R-PIR primary side, DC resistance, frequency-dependent resistance, capacitance of the R-PIR primary terminal, and the maximum impedance values of R-PIR's primary terminal. Fig. 17 presents the FS measurement of the R-PIR's capacitance between the primary and secondary terminal for the open-circuit state.

B. R-PIR Short-Circuit Test

For this test scenario, the secondary of the R-PIR is short-circuited. This configuration removes the magnetization and secondary capacitance of the R-PIR; the remaining elements are the leakage inductances ($L_{l1} + L_{l2}$), resistances (R_{dc1} and R_{dc2}), and primary capacitance (C_1).

As can be seen in Fig. 18, the resonance point is shifted to almost 20 MHz because of the decreased value of R-PIR inductance. The results of this test are presented in Table III.

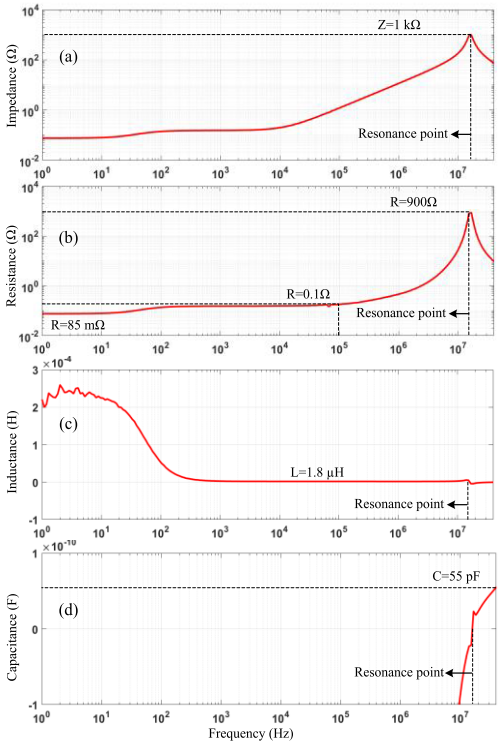

Fig. 18. The R-PIR short-circuit FS a) terminal impedance, b) terminal resistance, c) terminal inductance, and d) terminal capacitance measurement.

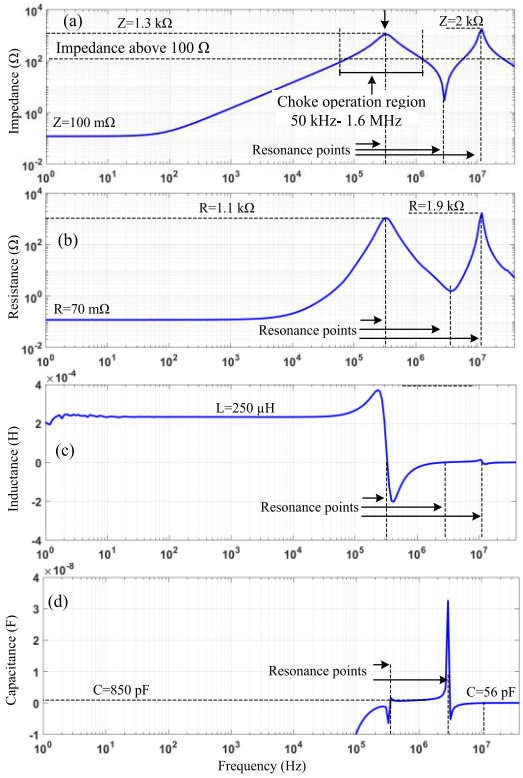

Fig. 19. R-PIR operation state FS a) terminal impedance, b) terminal resistance, c) terminal inductance, and d) terminal capacitance measurement.

TABLE IV

R-PIR PARAMETERS FOR THE OPERATING MODE TEST

Operating mode FS measurement						
Measured parameter	L_m	C_1	C_2	R	R (100 kHz)	Z_c (max)
parameter value	250 µH	56pF	78pF	100 mΩ	20 Ω	2 kΩ

Considering the measured data, it can be concluded that the frequency-dependent resistor does not grow significantly in the high-frequency region.

C. R-PIR Operating Mode Test

For the final experimental test defined as R-PIR operating mode, frequency sweep (FS) measurements of the primary terminal are performed with the secondary side connected to a resistor.. The measured results are shown in Fig. 19. According to Fig. 19(a), the operating range of the R-PIR is from 50 kHz to 1.8 MHz, where its total impedance remains above 100 Ω. The measured data are also summarized in Table IV.

D. Validation of the R-PIR Parameters

Based on the measurements performed in Section VI, all the parameters of the R-PIR can be accurately determined and compared to those obtained by FEM analysis and analytical formulas derived in Section III. Table V summarizes these results.

TABLE V

VALIDATION OF THE R-PIR PARAMETERS

Parameter	L_m	L_{l1}	L_{l2}	C_1	C_2	C_{12}	R_{dc1}	R_{dc2}	R_f
Measurement	255 µH	0.9 µH	0.9 µH	56 pF	78 pF	60 pF	70 mΩ	15 mΩ	30 mΩ
FEM	259 µH	0.8 µH	0.8 µH	56 pF	80 pF	68 pF	65 mΩ	12 mΩ	27 mΩ
Calculation	260 µH	0.8 µH	0.8 µH	55 pF	79 pF	67 pF	65 mΩ	14 mΩ	28 mΩ

E. Impulse Test of the R-PIR Prototype

To validate the operation of the R-PIR and its performance in reducing the magnitude of the transient voltage oscillation, an impulse test is carried out where the R-PIR is connected in series with a 10 kV, 200 VA transformer. The peak value of the impulse voltage is 10 kV. Fig. 20 shows the test setup, which is configured similarly to Fig. 1b. Fig. 21 shows the applied impulse voltage (blue curve), the voltage on the transformer terminal (red curve), and the voltage drop across the R-PIR(purple curve). It is clearly shown that the R-PIR contributes to a considerable decrease in the transformer voltage.

It can also be seen that the peak value of the transformer terminal voltage decreases by 20% (from 10 kV to 8 kV), and its rate of rise drops from 25 kV/μs to 20 kV/μs. Moreover, considering the R-PIR voltage drop during the impulse test, the R-PIR suppresses almost 40% of the average voltage, which is measured by the oscilloscope.

The performed analysis of the R-PIR shows the main advantages of the R-PIR compared to the mature state-of-the-art solutions, such as the surge arrester [7], the snubber [8], and the serial ring core [16]. Apart from transient overvoltage suppression, other advantages are in terms of power consumption during steady-state operation (PCSS), the effects on transient

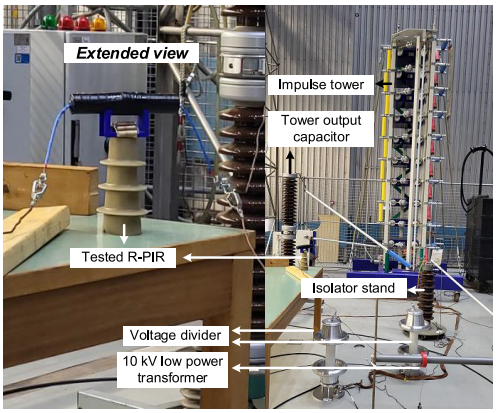

Fig. 20. High-voltage test setup to study the R-PIR performance.

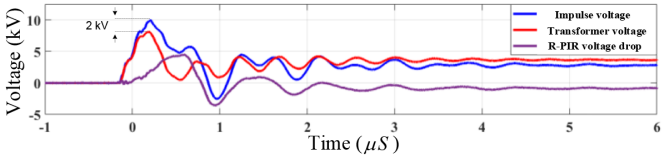

Fig. 21. Measured transient oscillation for the R-PIR test.

TABLE VI
R-PIR ADVANTAGES COMPARED TO OTHER SOLUTIONS

Features	Arrester [7]	Surge capacitor [8]	Series rings [19]	R-PIR
PCSS	High active power loss in transmission voltage level	High reactive power consumption in transmission voltage level	High reactive power consumption in high current line	Low active and reactive power consumption
EOTO	Chopping overvoltages	Filtering transient oscillations	Filtering transient oscillations	Filtering transient oscillation
VLSS	Grid voltage	Grid voltage	Almost zero	Almost zero
GR	Required grounding	Required grounding	Does not require grounding	Does not require grounding
TFR	No tunning possibility	No tunning possibility	No tunning possibility	Tuning possibility

oscillation (EOTO), the voltage level during the steady-state operation (VLSS), grounding requirement (GR), and tunable frequency response (TFR). These advantages are summarized in TABLE VI.

Comparative analysis presented in Table VI shows the good performance of R-PIR, as a new protection device against fast transient oscillations. The effect during steady-state operation is negligible, and during fast transient oscillations, R-PIR behaves as a filter that successfully suppresses a large amount of the transient signal without specific grounding requirements. Another advantage is the possibility of R-PIR being tuned and designed for different system configurations and voltage levels.

VII. CONCLUSION

This paper deals with the design of an R-PIR, a device to protect transformers against transient and resonance overvoltages. Firstly, parametric equations derived from the equivalent circuit of the R-PIR are presented. Subsequently, the R-PIR is modeled by applying FEM analysis, and its parameters are accurately calculated to evaluate the performance of the R-PIR. Considering the calculated parameters and the equivalent circuit of the R-PIR, an FS simulation is performed in EMTP to demonstrate the frequency-dependent impedance behavior of the R-PIR. The R-PIR parameters are measured using a laboratory test setup based on the FS analysis. These measurements validate the analysis conducted by FEM and EMTP. Obtained results show that R-PIR can provide a maximum of 1.3 kΩ in series against transient oscillation to suppress it. Furthermore, a high-voltage laboratory test circuit consisting of a transformer connected to the designed R-PIR is built. The performance of the R-PIR is tested by applying a standard lightning impulse of 10 kV, 1.2/50 us.

The investigation shows that the designed R-PIR successfully suppresses transient overvoltage peak magnitude from 10 kV to 8 kV, protects the transformers accordingly, and declines 40% of the transient oscillation average magnitude. Finally, the main outcome of this research work is how to build an R-PIR accurately to ensure robust transformer overvoltage protection against FT.

REFERENCES

[1] M. Popov and E. Acha, "Overvoltages due to switching off an unloaded transformer with a vacuum circuit breaker," *IEEE Trans. Power Del.*, vol. 14, no. 4, pp. 1317–1326, Oct. 1999.

[2] M. Hori et al., "Internal winding failure due to resonance overvoltage in distribution transformer caused by winter lightning," *IEEE Trans. Power Del.*, vol. 21, no. 3, pp. 1600–1606, Jul. 2006.

[3] A. H. Soloot, H. K. Høidalen, and B. Gustavsen, "Influence of the winding design of wind turbine transformers for resonant overvoltage vulnerability," *IEEE Trans. Dielectr. Electr. Insul.*, vol. 22, no. 2, pp. 1250–1257, Apr. 2015.

[4] *CSV Consolidated Version—Electromagnetic Compatibility (EMC)—Part 4–5: Testing and Measurement Techniques—Surge Immunity Test*, Standard IEC 61000-4-5:2014+AMD1:2017, 2017.

[5] T. Abdulahović and T. Thiringer, "Voltage stress in a transformer winding during very fast transients caused by breaker closing event," *IEEE Trans. Power Del.*, vol. 29, no. 4, pp. 1946–1954, Aug. 2014.

[6] P. Akiki, A. Xémard, C. Trouilloud, and J.-L. Chanelière, "Study of high frequency transient overvoltage caused by cable-transformer quarter-wave resonance," *Electr. Power Syst. Res.*, vol. 197, Aug. 2021, Art. no. 107295.

[7] M. A. Atefi, M. Sanaye-Pasand, and S. Bahari, "Preventing transformer energizing resonant overvoltages using surge arrester temperature rise index and controlled closing method," *IEEE Trans. Power Del.*, vol. 28, no. 2, pp. 998–1006, Apr. 2013.

[8] T. Dionise and S. Johnston, "Surge protection for ladle melt furnaces: LMF transformer terminals were equipped with primary surge protection consisting of surge arresters and RC snubbers," *IEEE Ind. Appl. Mag.*, vol. 21, no. 5, pp. 43–52, Sep. 2015.

[9] *Zinc Oxide RC-Surge Suppressor (ZORC) Capacitors, for HV-Motor and Transformers*. [Online]. Available: https://www.vishay.com/docs/13192/zoasurge.pdf

[10] K. Munji, J. Horne, and J. Ribecca, "Design and validation of pre-insertion resistor rating for mitigation of zero missing phenomenon," in *Proc. Int. Conf. Power Syst. Transients (IPST)*, 2017, pp. 26–29.

[11] H. Heiermeier and R. B. Raysaha, "Power testing of preinsertion resistors: Limitations and solution," *IEEE Trans. Power Del.*, vol. 32, no. 4, pp. 1688–1695, Aug. 2017.

[12] L. Zhou, L. Huang, R. Wei, and D. Wang, "A novel lightning overvoltage protection scheme using magnetic rings for transmission line systems," *IEEE Trans. Ind. Electron.*, vol. 70, no. 12, pp. 12872–12882, Dec. 2023.

[13] S. M. Korobeynikov, S. I. Krivosheev, S. G. Magazinov, V. A. Loman, and N. Ya, "Suppression of incoming high-frequency overvoltage in transformer coils," *IEEE Trans. Power Del.*, vol. 36, no. 5, pp. 2988–2994, Oct. 2021.

[14] D. Smugała et al., "Distribution transformers protection against high frequency switching transients," *Przegląd Elektrotechniczny (Elect. Rev.)*, 2012. [Online]. Available: http://www.red.pe.org.pl/articles/2012/5a/71.pdf

[15] D. Smugała et al., "New approach to protecting transformers against high frequency transients–wind turbine case study," *Prz. Elektrotech*, vol. 89, pp. 186–190, Oct. 2013.
[16] D. Smugala, W. Piasecki, M. Ostrogorska, M. Florkowski, M. Fulczyk, and O. Granhaug, "Wind turbine transformers protection method against high-frequency transients," *IEEE Trans. Power Del.*, vol. 30, no. 2, pp. 853–860, Apr. 2015, doi: 10.1109/TPWRD.2014.2343261.
[17] F. Nasirpour, A. Heidary, M. G. Niasar, A. Lekić, and M. Popov, "High-frequency transformer winding model with adequate protection," *Electr. Power Syst. Res.*, vol. 223, Oct. 2023, Art. no. 109637.
[18] S. Ghasemi, M. Allahbakhshi, B. Behdani, M. Tajdinian, and M. Popov, "Probabilistic analysis of switching transients due to vacuum circuit breaker operation on wind turbine step-up transformers," *Electr. Power Syst. Res.*, vol. 182, May 2020, Art. no. 106204.
[19] A. Heidary, M. G. Niasar, M. Popov, and A. Lekic, "Transformer resonance: Reasons, modeling approaches, solutions," *IEEE Access*, vol. 11, pp. 58692–58704, 2023.
[20] S. Burow, W. Köhler, S. Tenbohlen, and U. Straumann, "Damping of VFTO by RF resonator and nanocrystalline materials," in *Proc. IEEE Electr. Insul. Conf. (EIC)*, Ottawa, ON, Canada, Jun. 2013, pp. 439–443, doi: 10.1109/EIC.2013.6554284.
[21] L. V. Bewley, *Travelling Waves on Transmission Lines*. New York, NY, USA: Dover, 1963.
[22] E. O. Taylor, Ed., *Power System Transients*. London, U.K.: George Newnes Ltd, 1954.
[23] W. Piasecki, G. Bywalec, M. Florkowski, M. Fulczyk, and J. Furgal, "New approach towards very fast transients suppression," in *Proc. IPST*, 2007, pp. 1–6.
[24] D. Smugala et al., "Very fast transient suppressing device," U.S. Patent 8 929 048 B2, 2015.

Amir Heidary (Senior Member, IEEE) was born in Tabriz, Iran, in 1987. He received the B.Sc. and M.Sc. degrees from the Electrical Engineering Department, IAU, Iran, in 2009 and 2020, respectively. He is currently pursuing the Ph.D. degree with Delft University of Technology (TU Delft). He was a Researcher of electrical applications with Eleprotect Company from 2012 to 2017. His research has been published in books, journal articles, and several patents. His research interests include power system protection, power electronics, magnetic-based power applications, smart grids, and fast transients. His invention was awarded to the Iranian Elite Committee in 2014.

Mohamad Ghaffarian Niasar (Member, IEEE) was born in Tehran, Iran, in 1984. He received the M.Sc. degree from the Sharif University of Technology, Tehran, in 2008, and the Ph.D. degree in electrical engineering from the Royal Institute of Technology (KTH), Stockholm, Sweden, in 2015. He is currently an Assistant Professor with the High Voltage Technology Group, Delft University of Technology, The Netherlands. His research interests include the aging of electrical insulation, HVDC insulation systems, partial discharges, high-voltage power electronics, high-frequency power transformers, power cables, and FEM modeling.

Marjan Popov (Fellow, IEEE) received the Ph.D. degree in electrical power engineering from Delft University of Technology, Delft, in 2002. In 1997, he was an Academic Visitor with the University of Liverpool, Liverpool, U.K., working at the Arc Research Group on modeling SF6 circuit breakers. He is a Chevening Alumnus. His research interests include future power systems, large-scale power system transients, intelligent protection for future power systems, and wide-area monitoring and protection. He is a member of Cigre and actively participated in WG C4.502 and WG A2/C4.39. In 2010, he received the prestigious Dutch Hidde Nijland Prize for extraordinary research achievements. He received the IEEE PES Prize Paper Award and the IEEE Switchgear Committee Award in 2011. He is an Associate Editor of *International Journal of Electrical Power and Energy Systems* (Elsevier). He is the Co-Editor-in-Chief of *Advances in Electrical Engineering, Electronics and Energy* (Elsevier's e-Prime Journal). In 2017, together with the Dutch utilities TenneT, Alliander, and Stedin, he founded Dutch Power System Protection Centre to promote research and education in power system protection.